

Navigating Potholes with Geometry-Aware Sharpness Minimization

Simon Dufort-Labbé
Mila, Université de Montréal

Mehrab Hamidi
Mila, Université de Montréal

Razvan Pascanu
Mila, Université de Montréal

Ioannis Mitliagkas
Mila, Université de Montréal

Damien Scieur
Samsung – SAIL Montreal
Mila, Université de Montréal

Aristide Baratin
Samsung – SAIL Montreal
Mila, Université de Montréal

Abstract

Sharpness-aware minimization (SAM) encourages flat minima by perturbing parameters along directions of high loss curvature, but treats all parameter directions uniformly, ignoring the underlying loss geometry. We introduce LLQR+SAM, which combines SAM with a learned preconditioner obtained from the recently proposed LLQR framework—a second-order method that recasts steepest descent as a layerwise linear-quadratic regulator problem. The preconditioner is updated sparsely and maintained as a slow exponential moving average, so it captures a smoothed, low-resolution picture of the loss landscape geometry. The SAM perturbation then operates on top of this learned geometry, probing curvature at a faster timescale. We show that this two-timescale structure is not merely a computational convenience: theoretically, the preconditioner amplifies the SAM escape signal in directions that are flat under the average geometry but locally sharp (“potholes”). Wide, flat basins, by contrast, remain stable. Empirically, LLQR+SAM gives consistent gains over both SAM and LLQR alone across standard vision and sequence modeling benchmarks, supporting the view that slow learned geometry and fast sharpness correction are genuinely complementary.

Preprint.

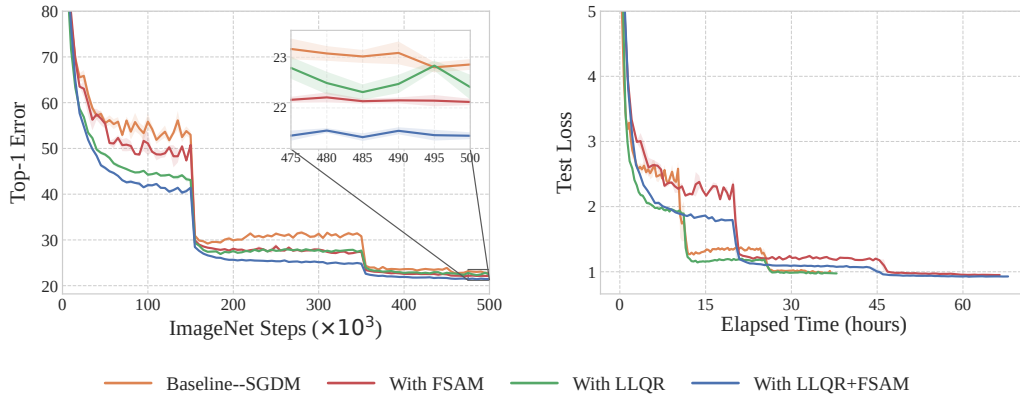


Figure 1: **Interaction between FSAM and LLQR on ResNet-50/ImageNet.** **Left:** Top-1 error for SGDM and FSAM, a SAM variant, with and without LLQR. Although both SAM-style methods and LLQR can be interpreted as curvature-correcting mechanisms, their combination yields gains over either component alone, suggesting complementary effects. **Right:** Test loss versus elapsed training time. Despite the usual concern that second-order methods are prohibitively expensive, LLQR remains efficient enough not to become the bottleneck: whenever the slowdown of SAM is acceptable, topping it with LLQR likely preserves affordability.

1 Introduction

Modern deep-learning loss landscapes are widely thought to combine smooth, slowly-varying structure at large scales—wide basins, valleys, and ridges shaped by the architecture and data—with much sharper features at smaller scales: narrow valleys, spurious minima, and localized *potholes* that act as attractors of poor generalization. Two largely independent lines of optimization research target these two scales. *Geometry-aware* methods such as natural gradient [Amari, 1998], Newton, K-FAC [Martens and Grosse, 2015] and Shampoo [Gupta et al., 2018] use estimates of curvature to reshape the descent direction, addressing the ill-conditioning of the average loss geometry. *Sharpness-aware* methods, beginning with SAM [Foret et al., 2021], perturb the parameters before evaluating the gradient, biasing optimization toward flatter minima.

These two mechanisms operate on different aspects of the geometry, and at very different time scales. A learned preconditioner accumulated over many gradient steps can only capture the slow average curvature of the landscape; it is by construction insensitive to sharp localized features. A SAM perturbation, evaluated on a single minibatch, probes local sharpness directly—but treats all parameter directions uniformly, ignoring the underlying optimization geometry. Each captures something the other misses.

In this work, we study the combination of the two. We use **LLQR** [Dufort-Labbé et al., 2026], a recently proposed framework that learns a structured inverse preconditioner U by minimizing a linear-quadratic-regulator (LQR) objective derived from the layerwise network dynamics and a chosen divergence on the loss. The preconditioner is updated sparsely (a few times per epoch) and maintained as an exponential moving average; it captures a smoothed, low-resolution picture of the average loss geometry. On top of this slow geometry we apply a SAM perturbation evaluated on each minibatch *in the U -induced norm*, and the resulting outer update uses the same learned geometry. The combined algorithm, **LLQR+SAM**, applies the SAM displacement and the gradient transport in a single learned metric.

Our central claim is that this two-time-scale combination is *synergistic*, not merely additive. We make this precise on a model landscape consisting of a quadratic loss with a smooth average geometry, supplemented by a sharp localized pothole that creates a spurious minimum invisible to U . On this landscape the LLQR+SAM dynamics is closed-form and exposes a clean mechanism: SAM prevents the iterate from settling at any minimum, forcing it to hover at the scale of the SAM probe itself, while U shapes that scale according to the average geometry. Around a wide basin the hovering is appropriate to the basin width and the iterate is stable; around a pothole the same hovering scale exceeds the pothole’s basin of attraction and the iterate escapes. Crucially, the escape signal is amplified relative to vanilla SAM by a factor that grows as the surrounding basin becomes flatter—precisely the regime where preconditioning matters most. The same U that enables fast convergence in flat directions also enables pothole escape: U and SAM are not independent ingredients but two complementary uses of one learned geometry. These predictions are borne out by the toy experiments in Figures 2 and 3 and by the empirical study of Section 5, which shows consistent gains over either component alone across CIFAR, TinyImageNet, ImageNet, and IWSLT14.

Contributions. (i) We propose LLQR+SAM, combining a slowly-updated, EMA-smoothed second-order preconditioner with a SAM perturbation evaluated in the induced geometry. (ii) On a quadratic landscape with a sharp pothole perturbation we derive the exact LLQR+SAM dynamics and quantify the escape-amplification of the preconditioner relative to vanilla SAM, with the gain growing as the surrounding basin becomes flatter. (iii) We validate empirically that the combination yields consistent gains over either component alone across standard vision and sequence benchmarks.

2 Related Work

Sharpness, flatness, and SAM. The relation between generalization and loss-landscape sharpness has long motivated methods that bias training toward flatter minima [Hochreiter and Schmidhuber, 1997, Keskar et al., 2017, Neyshabur et al., 2015], although this connection is neither universal nor invariant: sharpness can change under reparameterization without changing the represented function [Dinh et al., 2017]. SAM [Foret et al., 2021] is the canonical sharpness-aware optimizer, replacing the training objective by a local min–max problem that probes the worst-case loss near the cur-

rent parameters and descends using the gradient at the perturbed point. Many variants modify either the perturbation neighborhood or the adversarial-point estimate: ASAM [Kwon et al., 2021] uses a scale-adaptive radius to reduce sensitivity to parameter rescaling, while Friendly SAM [Li et al., 2024] reduces minibatch-noise sensitivity by averaging perturbation information across batches. A complementary view comes from gradient-norm penalization: Zhao et al. [2022] argue that penalizing the gradient norm encourages smaller local Lipschitz constants and show that SAM can be recovered as a special case of a loss augmented by a gradient-norm regularizer.

Geometry-aware sharpness neighborhoods. Vanilla SAM defines sharpness through Euclidean neighborhoods in parameter space, which may poorly reflect the effective geometry of neural networks [Li et al., 2018]. Fisher SAM addresses this by replacing the Euclidean ball with an ellipsoid induced by the Fisher information matrix, so the adversarial probe is measured in a geometry tied to the model distribution [Kim et al., 2022]. Riemannian SAM further generalizes this idea by defining the sharpness neighborhood through an arbitrary Riemannian metric [Yun and Yang, 2023]. In this view, Fisher SAM is a special case, and sharpness-aware perturbations are interpreted as steepest-ascent directions under a non-Euclidean local norm.

Geometry-aware optimization and robustness. A separate line of work uses geometry to transport gradients rather than to define adversarial neighborhoods. Natural-gradient descent defines steepest descent with respect to the Fisher information metric [Amari, 1998]. K-FAC makes this principle scalable through layerwise Kronecker-factored Fisher approximations [Martens and Grosse, 2015], while Shampoo maintains tensor-structured preconditioners along parameter dimensions [Gupta et al., 2018]. These methods use curvature estimates to precondition the optimization trajectory, but they do not introduce a SAM-style local adversarial probe. Another related direction controls sensitivity to input perturbations rather than parameter perturbations: spectral normalization and Lipschitz regularization reduce the local sensitivity of the network function to data-space changes [Yoshida and Miyato, 2017, Virmaux and Scaman, 2018]. Thus, while geometry-aware optimizers act on the parameter-space training dynamics and Lipschitz methods target input-space robustness, sharpness-aware methods study loss variation under parameter perturbations.

3 Method

Metric and notation. Let $L : \mathbb{R}^d \rightarrow \mathbb{R}$ denote the training loss, with $g(\theta) := \nabla L(\theta)$ and $H(\theta) := \nabla^2 L(\theta)$. We write $P(\theta) \succ 0$ for a local optimization metric and $U(\theta) := P(\theta)^{-1}$ for its inverse. The associated dual norm on gradients is

$$\|g\|_U := (g^\top U g)^{1/2}.$$

LLQR inverse metric. The LLQR framework [Dufort-Labbé et al., 2026] (See Appendix A) learns a structured inverse preconditioner U from layerwise network dynamics and a divergence on the loss, such as KL/Fisher or Newton/Bregman. In practice, U is represented by diagonal or K-FAC blocks, trading expressivity for cost. It is updated only every $n_{\text{LLQR}} \sim 500$ optimizer steps and smoothed by an exponential moving average, so applying U during training is a structured matrix-vector product with modest overhead. For the analysis in Section 4, the relevant properties are that U_t is positive definite, uniformly spectrally bounded, and frozen during each perturb-and-recompute step.

Euclidean SAM. Standard SAM [Foret et al., 2021] evaluates the update gradient at the worst-case first-order perturbation in a Euclidean ball:

$$\theta^+ = \theta + \rho \frac{g(\theta)}{\|g(\theta)\|_2}, \quad \theta \leftarrow \theta - \eta g(\theta^+).$$

LLQR+SAM. LLQR+SAM replaces the Euclidean perturbation geometry by the learned metric $P = U^{-1}$ and uses the same inverse metric to transport the outer gradient:

$$\theta^+ = \theta + \rho \frac{U g(\theta)}{\|g(\theta)\|_U}, \quad \theta \leftarrow \theta - \eta U g(\theta^+). \quad (1)$$

The perturbation is therefore the normalized steepest-ascent direction under the metric P , while the descent step applies the same geometry to the gradient evaluated at the perturbed point.

Algorithm 1 LLQR+SAM

- 1: **Input:** initial parameters θ_0 , learning rate η , SAM radius ρ , LLQR metric state, damping and update schedule.
 - 2: **for** $t = 0, 1, 2, \dots$ **do**
 - 3: Draw minibatch b_t and compute $g_t = \nabla_{\theta} L_{b_t}(\theta_t)$.
 - 4: Update or query the slow LLQR state to obtain $U_t \approx P_t^{-1}$.
 - 5: Set $\epsilon_t = \rho U_t g_t / (g_t^\top U_t g_t)^{1/2}$.
 - 6: Form the probe parameters $\theta_t^+ = \theta_t + \epsilon_t$.
 - 7: Compute the sharpness-aware gradient $\tilde{g}_t = \nabla_{\theta} L_{b_t}(\theta_t^+)$.
 - 8: Apply the geometry-aware update $\theta_{t+1} = \theta_t - \eta U_t \tilde{g}_t$.
 - 9: **end for**
 - 10: **Output:** trained parameters θ_T .
-

Interpretation. Equation (1) can be viewed locally as a Riemannian SAM step in the LLQR metric, with U_t fixed during the perturb-and-recompute step. The corresponding fixed-metric transfer from Riemannian SAM [Yun and Yang, 2023] gives stationarity in the instantaneous metric; Appendix B.1 gives the formal statement. This also separates LLQR+SAM from Fisher SAM [Kim et al., 2022]: Fisher SAM uses a Fisher-scaled perturbation to probe sharpness, but typically applies the resulting gradient with the base optimizer. LLQR+SAM instead uses the learned inverse metric U_t both to define the perturbation neighborhood and to transport the outer gradient. This coupling is central to the pothole-escape mechanism analyzed in Section 4: the amplification depends on the metric acting on both the probe and the descent step.

Algorithm 1 states the core update without momentum, weight decay, or optimizer-specific book-keeping. In implementation, these terms are composed around the same two operations: use the current LLQR state to define the perturbation geometry, then apply the preconditioned sharpness-aware gradient through the geometry-aware base update.

The wall-clock overhead of LLQR+SAM relative to the corresponding non-SAM, non-preconditioned run is approximately one extra forward/backward pass per step (the SAM probe), plus the cost of refreshing and applying the LLQR preconditioner. As shown in Fig. 1 (right), this additional geometry does not become the bottleneck in practice: when the cost of SAM is acceptable, adding LLQR preserves the same affordability regime while yielding stronger accuracy. For reproducibility, the implementation is available at github.com/SimonDufLab/LLQR.

4 Analysis: pothole navigation in a two-scale landscape

We analyze LLQR +SAM on a minimal two-scale quadratic model: an average geometry tracked by LLQR, plus a sharp localized perturbation not captured by the slowly updated preconditioner.

Two-scale model. Place a local minimum at the origin and consider

$$L(\theta) = \frac{1}{2} \theta^\top H \theta, \quad H = \bar{H} + H_\epsilon, \quad H \succ 0, \quad (2)$$

where $\bar{H} \succ 0$ encodes the smooth, slowly-varying part of the geometry and $H_\epsilon \succeq 0$ is a localized sharp component. We make the following modeling assumption, motivated by the slow, exponential moving average smoothed nature of the LLQR preconditioner.

Assumption 4.1. The LLQR inverse metric captures the average geometry: $U = \bar{H}^{-1}$.

For simplicity, assume that \bar{H} and H_ϵ share the same eigenbasis. Define

$$\lambda_i = \bar{\lambda}_i + \lambda_{\epsilon,i}, \quad \mu_i := \lambda_i \bar{\lambda}_i^{-1} = 1 + \lambda_{\epsilon,i} \bar{\lambda}_i^{-1}.$$

Thus $\mu_i \approx 1$ in average directions and $\mu_i \gg 1$ in pothole directions. The non-commuting case is handled by whitening with $\bar{H}^{-1/2}$; see Appendix B.2.

Dynamics. For (2), $g(\theta) = H\theta$, the LLQR+SAM recursion is exact for the quadratic loss (no Taylor approximation; see Appendix B.3):

$$e_{t+1} = (I - \eta UH)e_t - \eta \rho \|He_t\|_U^{-1} U H U H e_t, \quad (3)$$

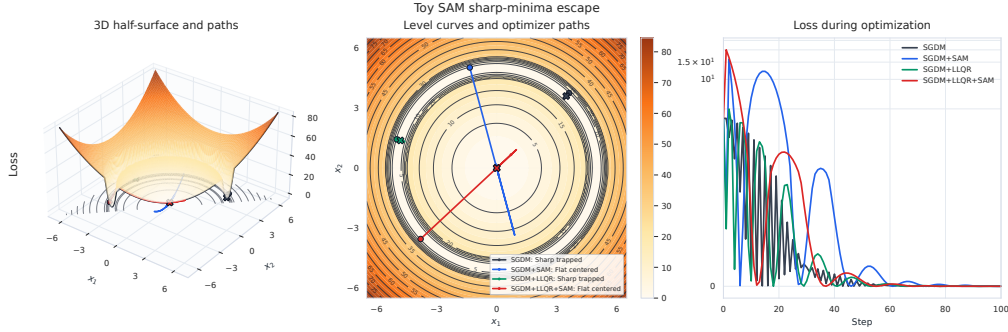


Figure 2: **Toy sharp-well escape mechanism.** The surface has a flat basin at the origin and a sharp annular basin near radius 5. All four optimizers use the same learning rate, and the SAM variants use the same radius, with starts chosen in the sharp basin, but not at minima. The non-SAM variants remain trapped, while the SAM variants leave the sharp well; the LLQR +SAM trajectory reaches the flat region with faster loss decay in this setting.

where $e_t = \theta_t$ is the displacement from the minimum. Restricted to a single eigendirection v_i (i.e., $e_t \propto v_i$),

$$z_{i,t+1} = (1 - \eta\mu_i)z_{i,t} - \eta\rho\mu_i\bar{\lambda}_i^{-1/2} \text{sign}(z_{i,t}), \quad z_{i,t} := \langle v_i, e_t \rangle. \quad (4)$$

Hovering and escape. The scalar map (4) has no nonzero fixed point: the SAM perturbation makes the iterate oscillate around the minimum instead of settling exactly at it. Its hovering envelope is

$$|z_{i,t}| \lesssim \rho\bar{\lambda}_i^{-1/2}, \quad (5)$$

with the exact two-cycle amplitude given in Appendix B.4. This scale comes from a cancellation: the SAM kick is of size $\eta\rho\mu_i\bar{\lambda}_i^{-1/2}$, while the contraction scale is $\eta\mu_i$, hence

$$\frac{\eta\rho\mu_i\bar{\lambda}_i^{-1/2}}{\eta\mu_i} = \rho\bar{\lambda}_i^{-1/2}.$$

Thus the hovering scale is controlled by the average curvature $\bar{\lambda}_i$, not by the localized sharpness $\lambda_{\epsilon,i}$. Consequently, if a pothole has basin radius r_ϵ , the iterate is no longer trapped in the pothole whenever

$$\rho\bar{\lambda}_\epsilon^{-1/2} > r_\epsilon. \quad (6)$$

Comparison with vanilla SAM. For vanilla SAM, the same calculation gives a Euclidean hovering envelope of order ρ in every direction; see Appendix B.6. Therefore LLQR +SAM amplifies the pothole-direction escape scale by $\bar{\lambda}_\epsilon^{-1/2}$.

Corollary 4.2 (Pothole-escape amplification; see Cor. B.2). *Under Assumption 4.1 and the commuting hypothesis, the LLQR +SAM hovering envelope around a pothole minimum is*

$$\rho\bar{\lambda}_\epsilon^{-1/2} = \bar{\lambda}_\epsilon^{-1/2} \times (\text{vanilla-SAM hovering envelope}).$$

The amplification depends only on the average curvature $\bar{\lambda}_\epsilon$ in the pothole direction.

Thus retuning vanilla SAM cannot reproduce the effect selectively: increasing ρ enlarges the probe in all directions, whereas LLQR +SAM uses the same $U \approx \bar{H}^{-1}$ for direction-adaptive probing and direction-adaptive contraction.

Toy illustrations. Figures 2 and 3 instantiate the mechanism on a two-dimensional sharp-well landscape. The non-SAM variants remain trapped, whereas SAM variants escape. With injected gradient noise, LLQR +SAM reaches the flat basin with shorter path length than vanilla SAM, consistent with Corollary 4.2. A stochastic selection model is given in Appendix B.7.

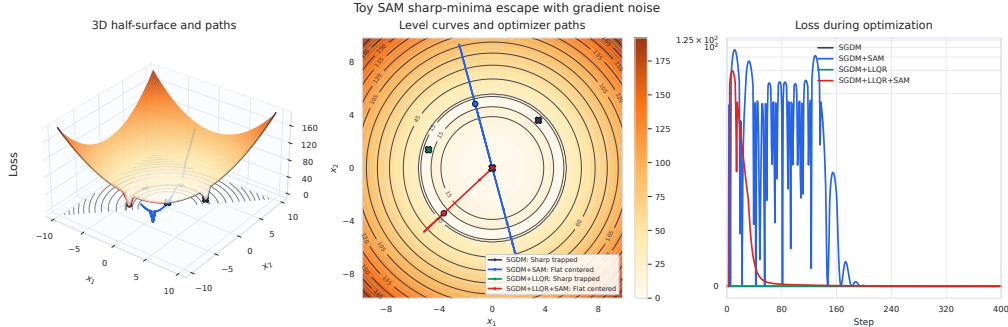


Figure 3: **Gradient-noise escape from the sharp minimum.** All variants start at the bottom of the sharp well and receive a shared deterministic Gaussian perturbation schedule in the update gradient. The non-SAM variants remain near the sharp well, while SAM variants are ejected. At variance 10^{-9} , both SAM variants reach the flat basin, but LLQR +SAM has substantially shorter path length than Euclidean SAM, consistent with the stochastic selection picture in Appendix B.7.

Table 1: CIFAR-10 standard supervised benchmark. Entries are best top-1 test accuracy (mean \pm std, 5 seeds). **Blue** denotes NGD-induced geometry, **Orange** denotes Newton-induced geometry.

Architecture	Base geometry			Sharpness baselines		Combined geometry and sharpness	
	SGDM	LLQR	LLQR	SAM	FISHERSAM	LLQR+SAM	LLQR+SAM
VGG16-BN	95.10 \pm 0.14	95.27 \pm 0.19	95.41 \pm 0.11	95.54 \pm 0.14	95.45 \pm 0.04	95.92 \pm 0.07	95.73 \pm 0.08
ResNet-18	96.14 \pm 0.19	96.37 \pm 0.11	96.37 \pm 0.11	96.65 \pm 0.16	96.74 \pm 0.14	96.85 \pm 0.09	96.78 \pm 0.03
WRN-28-10	96.94 \pm 0.09	97.04 \pm 0.08	97.10 \pm 0.03	97.43 \pm 0.09	97.41 \pm 0.04	97.64 \pm 0.08	97.52 \pm 0.07
PyramidNet-110	97.18 \pm 0.17	97.21 \pm 0.08	97.26 \pm 0.10	97.63 \pm 0.09	97.57 \pm 0.12	97.86 \pm 0.04	97.66 \pm 0.08

Stochastic counterpart: selection between wells. The deterministic analysis above shows that pothole minima are not attracting fixed points of LLQR+SAM. Under stochastic gradients this refines into a *selection* statement: sharp wells are short-lived (entered briefly through gradient noise, exited through the SAM kick), while flat wells support long visits. The same hovering-vs-basin comparison (6) controls the expected exit time, with LLQR+SAM benefiting from the amplification of Corollary 4.2. We give the regenerative model and the exit-time bound in Appendix B.7; the gradient-noise toy of Figure 3 is consistent with the prediction that LLQR+SAM exits the sharp well faster than vanilla SAM and reaches the flat basin with a markedly shorter path length.

5 Experiments

In this section, we evaluate LLQR+SAM on standard supervised vision benchmarks (CIFAR-10/100, TinyImageNet, ImageNet), a sequence-modeling task (IWSLT14 De-En), and a scalability study on ViT models up to ViT-Large/16. Throughout, LLQR+SAM reuses the hyperparameters of its LLQR and SAM components without method-specific retuning, isolating the effect of the geometry-sharpness coupling. Full training protocols are deferred to Appendix C. Additional experiments about noise injection and method scalability are presented in Appendix D.

5.1 Standard Supervised Training Benchmarks

CIFAR Datasets. We first evaluate the method on CIFAR-10 and CIFAR-100 [Krizhevsky and Hinton, 2009] with VGG16-BN [Simonyan and Zisserman, 2015], ResNet-18 [He et al., 2016], WRN-28-10 [Zagoruyko and Komodakis, 2016], and PyramidNet-110 [Han et al., 2017]; the full protocol is deferred to Appendix C.1. Tables 1 and 2 show that LLQR+SAM consistently improves over either component alone, indicating that coupling SAM with the learned LLQR geometry is more effective than applying either mechanism in isolation. Across CIFAR-10 and CIFAR-100, the NGD variant delivers the strongest results, suggesting that the natural-gradient geometry provides the more effective steepest descent metric in those setups.

TinyImageNet. We next scale the ResNet family networks to TinyImageNet-200 to test whether the geometry-sharpness coupling remains effective beyond CIFAR. Table 3 shows that the CIFAR

Table 2: CIFAR-100 standard supervised benchmark. Entries are best top-1 test accuracy (mean \pm std, 5 seeds). **Blue** denotes NGD-induced geometry, **Orange** denotes Newton-induced geometry.

Architecture	Base geometry			Sharpness baselines		Combined geometry and sharpness	
	SGDM	LLQR	LLQR	SAM	FISHERSAM	LLQR+SAM	LLQR+SAM
VGG16-BN	75.65 \pm 0.28	76.32 \pm 0.35	76.31 \pm 0.11	76.70 \pm 0.18	76.70 \pm 0.10	78.14 \pm 0.27	77.67 \pm 0.27
ResNet-18	79.27 \pm 0.18	79.53 \pm 0.39	79.83 \pm 0.18	81.13 \pm 0.21	80.89 \pm 0.31	81.82 \pm 0.14	81.65 \pm 0.10
WRN-28-10	82.50 \pm 0.18	82.80 \pm 0.37	82.72 \pm 0.24	84.83 \pm 0.06	84.71 \pm 0.13	85.30 \pm 0.14	85.05 \pm 0.12
PyramidNet-110	83.96 \pm 0.25	84.40 \pm 0.46	84.00 \pm 0.16	86.20 \pm 0.18	85.92 \pm 0.10	86.67 \pm 0.21	86.53 \pm 0.05

Table 3: TinyImageNet-200 ResNet-family benchmark. Entries are best top-1 test accuracy (mean \pm std, 3 seeds). **Blue** denotes NGD-induced geometry, **Orange** denotes Newton-induced geometry.

Architecture	Base geometry			Sharpness baseline	Combined geometry and sharpness	
	SGDM	LLQR	LLQR	SAM	LLQR+SAM	LLQR+SAM
ResNet-18	57.97 \pm 0.28	57.02 \pm 0.49	57.62 \pm 0.47	61.17 \pm 0.27	62.24 \pm 0.49	61.98 \pm 0.22
WRN-28-10	61.06 \pm 0.37	60.08 \pm 0.32	60.37 \pm 0.33	63.91 \pm 0.41	64.65 \pm 0.51	64.59 \pm 0.25

trend persists when scaling to TinyImageNet. SAM gives a strong gain over SGDM, while LLQR alone is not sufficient or not well-tuned in this setting. Yet, the combined LLQR+SAM variants improve over SAM on both architectures, with the NGD-induced geometry giving the best result in each case. This is a particularly stringent test of complementarity: even when LLQR alone does not improve over SGDM, its geometry still strengthens SAM, suggesting that the learned geometry provides useful information that is not captured by the sharpness perturbation alone.

Synergy with SAM variants. The SAM framework has led to a broad family of perturb-and-recompute optimizers, many differing only in how the adversarial direction is filtered or normalized. To check that LLQR is not merely tuned to vanilla SAM, we pair it with F-SAM [Li et al., 2024], a strong SAM variant. Performance is compared with and without the learned LLQR geometry, using vanilla SAM as a reference in Table 4.

ImageNet. We also extend the comparison to ResNet-50 on ImageNet [Deng et al., 2009]. As shown in Table 5, adding LLQR to F-SAM again improves performance over the sharpness-aware baseline. The full top-1 error trajectory in Fig. 1 (left) makes the effect even clearer: the paired method not only reaches better generalization, but also converges faster across early and mid training. These results suggest that LLQR and SAM-family pairing synergize throughout the entire training process, even at ImageNet scale.

IWSLT14 German-to-English. To assess if the geometry-sharpness coupling transfers beyond vision, we evaluate on the fairseq IWSLT14 German-to-English Transformer benchmark. As shown in Table 6, the gains are more modest than in image classification, but LLQR+SAM still achieves the best BLEU. More strikingly, the convergence curves in Fig. 4 show faster optimization when

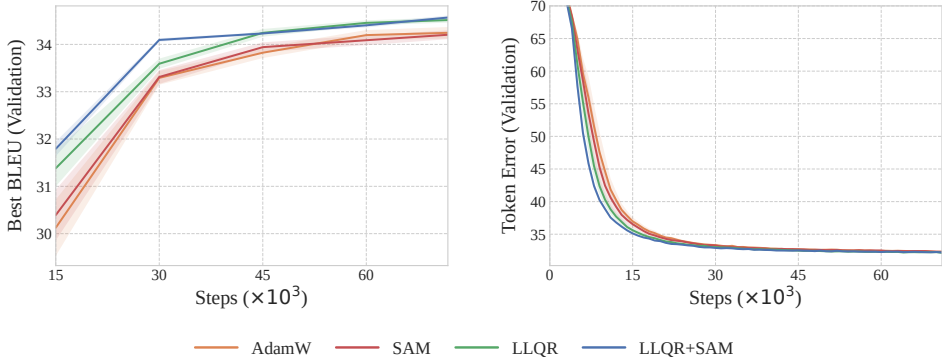


Figure 4: **IWSLT14 German-to-English convergence.** Validation BLEU and token error curves for the fairseq Transformer benchmark. Pairing LLQR with SAM accelerates optimization while offering the modest best-performance gains reported in Table 6

Table 4: CIFARs Friendly-SAM synergy benchmark. Entries are best top-1 test accuracy (mean \pm std, 5 seeds). **Blue** denotes NGD-induced LLQR geometry.

Dataset	Architecture	Without LLQR		With LLQR geometry	
		SAM	F-SAM	LLQR+SAM	LLQR +F-SAM
CIFAR-10	VGG16-BN	95.54 \pm 0.14	95.58 \pm 0.09	95.92 \pm 0.07	95.81 \pm 0.11
CIFAR-10	ResNet-18	96.65 \pm 0.16	96.60 \pm 0.05	96.85 \pm 0.09	96.88 \pm 0.11
CIFAR-10	WRN-28-10	97.43 \pm 0.09	97.49 \pm 0.08	97.64 \pm 0.08	97.68 \pm 0.07
CIFAR-10	PyramidNet-110	97.63 \pm 0.09	97.65 \pm 0.07	97.86 \pm 0.04	97.89 \pm 0.06
CIFAR-100	VGG16-BN	76.70 \pm 0.18	76.95 \pm 0.32	78.14 \pm 0.27	78.22 \pm 0.31
CIFAR-100	ResNet-18	81.13 \pm 0.21	81.16 \pm 0.12	81.82 \pm 0.14	82.00 \pm 0.28
CIFAR-100	WRN-28-10	84.83 \pm 0.06	84.86 \pm 0.16	85.30 \pm 0.14	85.21 \pm 0.20
CIFAR-100	PyramidNet-110	86.20 \pm 0.18	86.23 \pm 0.08	86.67 \pm 0.21	86.76 \pm 0.13

Table 5: ImageNet/ResNet-50 benchmark. Entries are best top-1 test accuracy (mean \pm std, 3 seeds). **Blue** denotes NGD-induced geometry, **Orange** denotes Newton-induced geometry. LLQR rows use the E-KFAC block structure.

Architecture	Base geometry			Sharpness baseline	Combined geometry and sharpness	
	SGDM	LLQR	LLQR	F-SAM	LLQR +F-SAM	LLQR +F-SAM
ResNet-50	77.60 \pm 0.31	78.05 \pm 0.12	76.93 \pm 0.42	77.92 \pm 0.07	78.61 \pm 0.16	78.19 \pm 0.14

LLQR and SAM are paired, extending the same pattern observed in vision to a sequence-modeling benchmark.

5.2 Isolating the role of geometry in probe and transport: FisherSAM Ablation

FisherSAM uses its geometry only to define the perturbation; LLQR+SAM additionally uses it to transport the outer update. To separate these two roles, we introduce LLQR $^{\Delta}$ +SAM, which applies the learned preconditioner only in the perturbation step (matching the FisherSAM pattern). On ResNet-18/CIFAR-100 (Table 7), LLQR $^{\Delta}$ +SAM already improves over FisherSAM—the LLQR geometry is itself a better probe—and full LLQR+SAM improves further, showing that transporting the outer update in the same geometry adds a separate gain.

5.3 Scalability

To assess scalability, we evaluate the computational and memory footprint of LLQR and LLQR+SAM on ViT models of increasing size [Dosovitskiy et al., 2021], from ViT-Tiny/16 to ViT-Large/16, on ImageNet-scale data. We compare LLQR and LLQR+SAM against SGD, AdamW, and SAM, measuring wall-clock time across update cadences. Figure 6 reports the steady preconditioner-update time as a function of model size: empirically, the recurring LLQR cost scales as $\mathcal{O}(P^{1.27-1.28})$ on the number of parameters P , closer to linear than to the quadratic scaling typically associated with second-order methods. Pairing LLQR with SAM does not change this scaling. Memory is controlled by the choice of preconditioner block structure (E-KFAC, K-FAC, diag-KFAC, diagonal, etc.); Appendix D.2 details the storage tradeoffs and reports the cadence sweep across update intervals. We also provide cadence results in Table 10 (Appendix D.2) and Fig. 5, to be read as wall-clock overhead measurements, not as accuracy or convergence comparisons. As expected, the cost decreases when LLQR updates are performed less frequently, since fewer preconditioner refreshes are executed per epoch. This steady-update scaling trend is further exposed in Fig. 6.

Table 7: ResNet-18/CIFAR-100 FisherSAM-style perturbation ablation. Entries are best top-1 accuracy (mean \pm std, five seeds). **LLQR $^{\Delta}$ +SAM** uses LLQR preconditioner only in the perturbation step, similar to FisherSAM.

Method	Top-1 accuracy
FISHERSAM	80.89 \pm 0.31
LLQR$^{\Delta}$+SAM	81.23 \pm 0.14
LLQR+SAM	81.82 \pm 0.14

Table 6: IWSLT14 German-to-English Transformer benchmark. Entries are best validation BLEU (mean \pm std, 5 seeds). **Blue** denotes NGD-induced LLQR geometry.

Dataset	Base geometry		Sharpness baseline	Combined geometry and sharpness
	ADAMW	LLQR	SAM	LLQR+SAM
IWSLT14 De-En	34.24 \pm 0.27	34.51 \pm 0.12	34.20 \pm 0.19	34.57 \pm 0.09

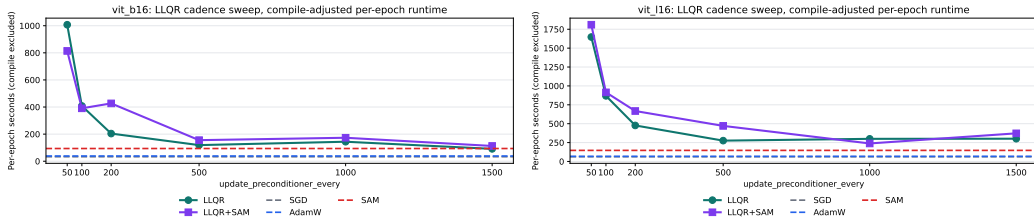


Figure 5: LLQR cadence sweep for ViT-B/16 and ViT-L/16. Each panel shows compile-adjusted seconds per epoch versus the LLQR update interval, with first-order baselines as horizontal references. Note that the ImageNet ResNet-50 runs in Fig. 1 use 1500-step updates.

6 Conclusion

We introduced LLQR+SAM, which pairs a slowly-updated LLQR preconditioner with a SAM perturbation evaluated and transported in the induced geometry. On a quadratic two-scale model the dynamics is closed-form: SAM prevents the iterate from localizing at any minimum, and the learned U shapes the hovering scale to match the average geometry—large enough to escape sharp potholes, small enough to stay inside wide basins. The pothole-direction probe is amplified relative to vanilla SAM by a factor that grows as the surrounding basin becomes flatter—the regime where preconditioning matters most. The same U that improves conditioning therefore also improves escape: U and SAM are not independent ingredients but two complementary uses of one learned geometry.

Empirically, LLQR+SAM yields consistent gains over either component alone across CIFAR-10/100, TinyImageNet, ImageNet, and IWSLT14, including when paired with stronger SAM variants such as F-SAM, and the per-step overhead remains close to first-order training across ViT scales.

Limitations Our analysis relies on an idealized two-timescale quadratic model in which the slow LLQR metric captures average geometry and the SAM perturbation probes localized sharpness. This setting is useful for exposing the mechanism, but it cannot certify that the same decomposition transfers cleanly to the highly nonconvex and stochastic regime of deep networks.

The empirical scope is also finite: we cover standard supervised vision benchmarks and one sequence-modeling task, but not large language model pre-training or fine-tuning, nor every architecture family.

Finally, LLQR+SAM inherits the extra gradient evaluation of SAM and adds periodic LLQR metric updates; while the resulting overhead is practical in our experiments, the best block structure, update cadence, and memory budget remain scale-dependent design choices.

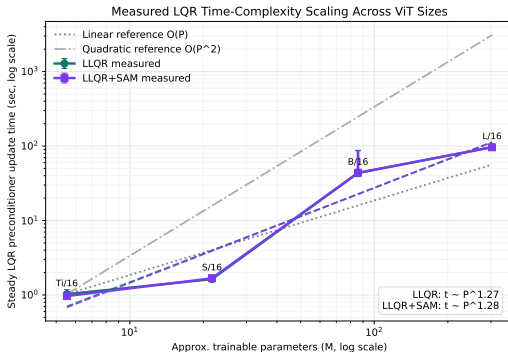


Figure 6: Across ViT scales, preconditioner-update time grows nearly linearly for both LLQR and LLQR+SAM, far from the quadratic scaling typically associated with second-order methods.

References

- Shun-ichi Amari. Natural gradient works efficiently in learning. *Neural Comput.*, 10(2): 251–276, 1998. doi: 10.1162/089976698300017746. URL <https://doi.org/10.1162/089976698300017746>.
- Jia Deng, Wei Dong, Richard Socher, Li-Jia Li, Kai Li, and Li Fei-Fei. Imagenet: A large-scale hierarchical image database. In *2009 IEEE Computer Society Conference on Computer Vision and Pattern Recognition (CVPR 2009), 20-25 June 2009, Miami, Florida, USA*, pages 248–255. IEEE Computer Society, 2009. doi: 10.1109/CVPR.2009.5206848. URL <https://doi.org/10.1109/CVPR.2009.5206848>.
- Terrance Devries and Graham W. Taylor. Improved regularization of convolutional neural networks with cutout. *CoRR*, abs/1708.04552, 2017. URL <http://arxiv.org/abs/1708.04552>.
- Laurent Dinh, Razvan Pascanu, Samy Bengio, and Yoshua Bengio. Sharp minima can generalize for deep nets. In *Proceedings of the 34th International Conference on Machine Learning, ICML 2017, Sydney, NSW, Australia, 6-11 August 2017*, Proceedings of Machine Learning Research, pages 1019–1028. PMLR, 2017. URL <http://proceedings.mlr.press/v70/dinh17b.html>.
- Alexey Dosovitskiy, Lucas Beyer, Alexander Kolesnikov, Dirk Weissenborn, Xiaohua Zhai, Thomas Unterthiner, Mostafa Dehghani, Matthias Minderer, Georg Heigold, Sylvain Gelly, Jakob Uszkoreit, and Neil Houlsby. An image is worth 16x16 words: Transformers for image recognition at scale. *9th International Conference on Learning Representations, ICLR 2021, Virtual Event, Austria, May 3-7, 2021*, 2021. URL <https://openreview.net/forum?id=YicbFdNTTy>.
- Simon Dufort-Labbé, Pierre-Luc Bacon, Razvan Pascanu, Simon Lacoste-Julien, and Aristeide Baratin. Layerwise lqr for geometry-aware optimization of deep networks, 2026. URL <https://arxiv.org/abs/2605.04230>.
- Pierre Foret, Ariel Kleiner, Hossein Mobahi, and Behnam Neyshabur. Sharpness-aware minimization for efficiently improving generalization. In *9th International Conference on Learning Representations, ICLR 2021, Virtual Event, Austria, May 3-7, 2021*. OpenReview.net, 2021. URL <https://openreview.net/forum?id=6Tm1mposlrM>.
- Vineet Gupta, Tomer Koren, and Yoram Singer. Shampoo: Preconditioned stochastic tensor optimization. In *Proceedings of the 35th International Conference on Machine Learning, ICML 2018, Stockholmsmässan, Stockholm, Sweden, July 10-15, 2018*, Proceedings of Machine Learning Research, pages 1837–1845. PMLR, 2018. URL <http://proceedings.mlr.press/v80/gupta18a.html>.
- Dongyoon Han, Jiwhan Kim, and Junmo Kim. Deep pyramidal residual networks. In *2017 IEEE Conference on Computer Vision and Pattern Recognition, CVPR 2017, Honolulu, HI, USA, July 21-26, 2017*, pages 6307–6315. IEEE Computer Society, 2017. doi: 10.1109/CVPR.2017.668. URL <https://doi.org/10.1109/CVPR.2017.668>.
- Kaiming He, Xiangyu Zhang, Shaoqing Ren, and Jian Sun. Deep residual learning for image recognition. In *2016 IEEE Conference on Computer Vision and Pattern Recognition, CVPR 2016, Las Vegas, NV, USA, June 27-30, 2016*, pages 770–778. IEEE Computer Society, 2016. doi: 10.1109/CVPR.2016.90. URL <https://doi.org/10.1109/CVPR.2016.90>.
- Sepp Hochreiter and Jürgen Schmidhuber. Flat minima. *Neural Comput.*, 9(1):1–42, 1997. doi: 10.1162/neco.1997.9.1.1. URL <https://doi.org/10.1162/neco.1997.9.1.1>.
- Nitish Shirish Keskar, Dheevatsa Mudigere, Jorge Nocedal, Mikhail Smelyanskiy, and Ping Tak Peter Tang. On large-batch training for deep learning: Generalization gap and sharp minima. In *5th International Conference on Learning Representations, ICLR 2017, Toulon, France, April 24-26, 2017, Conference Track Proceedings*. OpenReview.net, 2017. URL <https://openreview.net/forum?id=H1oyRlygg>.
- Minyoung Kim, Da Li, Shell Xu Hu, and Timothy M. Hospedales. Fisher SAM: information geometry and sharpness aware minimisation. *International Conference on Machine Learning, ICML 2022, 17-23 July 2022, Baltimore, Maryland, USA*, pages 11148–11161, 2022. URL <https://proceedings.mlr.press/v162/kim22f.html>.

- Alex Krizhevsky and Geoffrey Hinton. Learning multiple layers of features from tiny images. Technical report, University of Toronto, 2009.
- Jungmin Kwon, Jeongseop Kim, Hyunseo Park, and In Kwon Choi. ASAM: adaptive sharpness-aware minimization for scale-invariant learning of deep neural networks. In *Proceedings of the 38th International Conference on Machine Learning, ICML 2021, 18-24 July 2021, Virtual Event, Proceedings of Machine Learning Research*, pages 5905–5914. PMLR, 2021. URL <http://proceedings.mlr.press/v139/kwon21b.html>.
- Bingcong Li and Georgios B. Giannakis. Enhancing sharpness-aware optimization through variance suppression. *Advances in Neural Information Processing Systems 36: Annual Conference on Neural Information Processing Systems 2023, NeurIPS 2023, New Orleans, LA, USA, December 10 - 16, 2023*, 2023.
- Hao Li, Zheng Xu, Gavin Taylor, Christoph Studer, and Tom Goldstein. Visualizing the loss landscape of neural nets. *Advances in Neural Information Processing Systems 31: Annual Conference on Neural Information Processing Systems 2018, NeurIPS 2018, December 3-8, 2018, Montréal, Canada*, pages 6391–6401, 2018.
- Tao Li, Pan Zhou, Zhengbao He, Xinwen Cheng, and Xiaolin Huang. Friendly sharpness-aware minimization. In *IEEE/CVF Conference on Computer Vision and Pattern Recognition, CVPR 2024, Seattle, WA, USA, June 16-22, 2024*, pages 5631–5640. IEEE, 2024. doi: 10.1109/CVPR52733.2024.00538. URL <https://doi.org/10.1109/CVPR52733.2024.00538>.
- James Martens and Roger B. Grosse. Optimizing neural networks with kronecker-factored approximate curvature. In *Proceedings of the 32nd International Conference on Machine Learning, ICML 2015, Lille, France, 6-11 July 2015, JMLR Workshop and Conference Proceedings*, pages 2408–2417. JMLR.org, 2015. URL <http://proceedings.mlr.press/v37/martens15.html>.
- Peng Mi, Li Shen, Tianhe Ren, Yiyi Zhou, Xiaoshuai Sun, Rongrong Ji, and Dacheng Tao. Make sharpness-aware minimization stronger: A sparsified perturbation approach. *Advances in Neural Information Processing Systems 35: Annual Conference on Neural Information Processing Systems 2022, NeurIPS 2022, New Orleans, LA, USA, November 28 - December 9, 2022*, 2022.
- Behnam Neyshabur, Ruslan Salakhutdinov, and Nathan Srebro. Path-sgd: Path-normalized optimization in deep neural networks. *Advances in Neural Information Processing Systems 28: Annual Conference on Neural Information Processing Systems 2015, December 7-12, 2015, Montreal, Quebec, Canada*, pages 2422–2430, 2015. URL <https://proceedings.neurips.cc/paper/2015/hash/eaa32c96f620053cf442ad32258076b9-Abstract.html>.
- Myle Ott, Sergey Edunov, David Grangier, and Michael Auli. Scaling neural machine translation. In *Proceedings of the Third Conference on Machine Translation: Research Papers, WMT 2018, Belgium, Brussels, October 31 - November 1, 2018*, pages 1–9. Association for Computational Linguistics, 2018. doi: 10.18653/V1/W18-6301. URL <https://doi.org/10.18653/v1/w18-6301>.
- Karen Simonyan and Andrew Zisserman. Very deep convolutional networks for large-scale image recognition. *3rd International Conference on Learning Representations, ICLR 2015, San Diego, CA, USA, May 7-9, 2015, Conference Track Proceedings*, 2015. URL <http://arxiv.org/abs/1409.1556>.
- Aladin Virmaux and Kevin Scaman. Lipschitz regularity of deep neural networks: analysis and efficient estimation. *Advances in Neural Information Processing Systems 31: Annual Conference on Neural Information Processing Systems 2018, NeurIPS 2018, December 3-8, 2018, Montréal, Canada*, pages 3839–3848, 2018.
- Yuichi Yoshida and Takeru Miyato. Spectral norm regularization for improving the generalizability of deep learning. *CoRR*, abs/1705.10941, 2017. URL <http://arxiv.org/abs/1705.10941>.
- Jihun Yun and Eunho Yang. Riemannian SAM: sharpness-aware minimization on riemannian manifolds. In Alice Oh, Tristan Naumann, Amir Globerson, Kate Saenko, Moritz Hardt, and Sergey Levine, editors, *Advances in Neural Information Processing Systems 36: Annual Conference on*

Neural Information Processing Systems 2023, NeurIPS 2023, New Orleans, LA, USA, December 10 - 16, 2023, 2023. URL http://papers.nips.cc/paper_files/paper/2023/hash/cf701db0e3b4d0b8681ca6915ac3e87e-Abstract-Conference.html.

Sergey Zagoruyko and Nikos Komodakis. Wide residual networks. In *Proceedings of the British Machine Vision Conference 2016, BMVC 2016, York, UK, September 19-22, 2016*. BMVA Press, 2016. URL <https://bmva-archive.org.uk/bmvc/2016/papers/paper087/index.html>.

Yang Zhao, Hao Zhang, and Xiuyuan Hu. Penalizing gradient norm for efficiently improving generalization in deep learning. *International Conference on Machine Learning, ICML 2022, 17-23 July 2022, Baltimore, Maryland, USA*, pages 26982–26992, 2022. URL <https://proceedings.mlr.press/v162/zhao22i.html>.

Contents

1	Introduction	2
2	Related Work	2
3	Method	3
4	Analysis: pothole navigation in a two-scale landscape	4
5	Experiments	6
5.1	Standard Supervised Training Benchmarks	6
5.2	Isolating the role of geometry in probe and transport: FisherSAM Ablation	8
5.3	Scalability	8
6	Conclusion	9
A	Layerwise LQR: Learning a Reusable Geometry	14
B	Detailed Analysis for the Two-Scale Pothole Model	16
B.1	Riemannian-SAM transfer under the frozen LLQR metric	16
B.2	Whitened form and non-commuting case	17
B.3	Coordinate recursion	17
B.4	Scalar Hovering Envelope	18
B.5	Pothole Escape Criterion	18
B.6	Vanilla SAM Comparison	18
B.7	Stochastic Selection Between Wells	19
C	Experiments Details	21
C.1	Standard Supervised Training Benchmarks	21
D	Additional Experimental Results	22
D.1	Noise injection robustness	22
D.2	Scalability	22

A Layerwise LQR: Learning a Reusable Geometry

We briefly summarize the Layerwise LQR (LLQR) methodology of Dufort-Labbé et al. [2026], which provides the geometry used throughout this work. The motivation is to obtain the benefits of second-order or natural-gradient descent without explicitly forming, storing, or inverting a global curvature matrix. At an iterate θ^k , a broad class of geometry-aware descent directions can be written as the solution of the local quadratic problem

$$\Delta\theta^* = \arg \min_{\Delta\theta} \left\{ \nabla L(\theta^k)^\top \Delta\theta + \frac{1}{2} \Delta\theta^\top H(\theta^k) \Delta\theta \right\}, \quad (7)$$

where H may be a regularized Hessian, Gauss–Newton matrix, Fisher matrix, or more general divergence-induced metric. Directly solving $H\Delta\theta = -\nabla L(\theta^k)$ is infeasible for modern networks, and standard scalable approximations typically impose block structure on H before solving the problem. LLQR instead first rewrites the dense quadratic problem as a layerwise optimal-control problem, and only later imposes structure on the learned inverse update.

Consider a depth- N network

$$x_{i+1} = f_i(x_i, \theta_i), \quad i = 0, \dots, N-1.$$

Linearizing the forward pass at (x_i^k, θ_i^k) gives the perturbation dynamics

$$\delta x_{i+1} = A_i \delta x_i + B_i \delta \theta_i, \quad \delta x_0 = 0, \quad (8)$$

with $A_i = \partial f_i / \partial x_i$ and $B_i = \partial f_i / \partial \theta_i$. For divergence-induced quadratic models, the global quadratic form in (7) can then be decomposed into layerwise costs

$$\delta x_N^\top Q_N \delta x_N + \sum_{i=0}^{N-1} \begin{bmatrix} \delta x_i \\ \delta \theta_i \end{bmatrix}^\top \begin{bmatrix} Q_i & M_i^\top \\ M_i & R_i \end{bmatrix} \begin{bmatrix} \delta x_i \\ \delta \theta_i \end{bmatrix},$$

subject to the linearized dynamics (8). The resulting problem is a finite-horizon Linear Quadratic Regulator: the network defines the dynamics, while the chosen descent geometry defines the quadratic costs. Its exact Riccati solution recovers the corresponding second-order update, including Newton, Gauss–Newton, and natural-gradient variants. In large networks, however, the exact Riccati recursion remains too expensive, so LLQR uses it as a reference objective rather than as the deployed optimizer.

The scalable relaxation parameterizes the update by a structured inverse preconditioner

$$\delta \theta_i = -U_i \nabla_{\theta_i} L(\theta^k), \quad U = \text{diag}(U_0, \dots, U_{N-1}),$$

Algorithm 2 LLQR: relaxed periodic preconditioner

Require: model f , loss L , data loader \mathcal{D} , outer optimizer \mathcal{O}_{out} , step size η

Require: recompute period n , inner steps T , structure \mathcal{S} , inner optimizer \mathcal{O}_{in} , inner step size α , EMA parameter β

- 1: Initialize θ^0 and $U \leftarrow I$ projected to \mathcal{S}
 - 2: **for** $k = 0, 1, 2, \dots$ **do**
 - 3: Sample minibatch $(x^k, y^k) \sim \mathcal{D}$ and compute $g_k \leftarrow \nabla_{\theta} L(\theta^k)$
 - 4: **if** $k \bmod n = 0$ **then**
 - 5: Linearize the network: $(A_i, B_i) \leftarrow (\nabla_x, \nabla_{\theta}) f_i(x_i^k, \theta_i^k)$
 - 6: Form the LQR blocks (Q_i, R_i, M_i) for the chosen divergence-induced metric
 - 7: Set $U_0 \leftarrow U$
 - 8: **for** $t = 0$ to $T - 1$ **do**
 - 9: $U_{t+1} \leftarrow \mathcal{O}_{\text{in}}(U_t, \nabla_{U_t} J, \alpha)$, where J is the relaxed objective (9)
 - 10: **end for**
 - 11: $U \leftarrow \beta U + (1 - \beta) U_T$
 - 12: **end if**
 - 13: Precondition the gradient: $\tilde{g}_k \leftarrow U g_k$
 - 14: Update parameters with the base optimizer: $\theta^{k+1} \leftarrow \mathcal{O}_{\text{out}}(\theta^k, \tilde{g}_k, \eta)$
 - 15: **end for**
-

where each U_i may be diagonal, Kronecker-factored, E-KFAC-like, or another structured block. Substituting this restricted update into the LQR objective yields a direct objective over U :

$$\begin{aligned} \min_U \quad & \nabla_{x_N} \ell(x_N)^\top \delta x_N + \frac{1}{2} \delta x_N^\top Q_N \delta x_N + \sum_{i=0}^{N-1} \left[\frac{1}{2} \delta x_i^\top Q_i \delta x_i + \frac{1}{2} \delta \theta_i^\top R_i \delta \theta_i + \delta \theta_i^\top M_i \delta x_i \right] \quad (9) \\ \text{s.t.} \quad & \delta x_{i+1} = A_i \delta x_i - B_i U_i \nabla_{\theta_i} L(\theta^k), \quad \delta x_0 = 0. \end{aligned}$$

Thus, structure is imposed on the reusable inverse action U , not on the curvature model before the layerwise objective is derived. This distinction is important for LLQR +SAM: the learned geometry still comes from a layer-coupled objective that encodes the dense quadratic model through the forward dynamics, while the deployed update only requires applying U to gradients.

In the LLQR +SAM setting, U should be viewed as a slowly updated transport geometry. Between preconditioner refreshes, it is held fixed and applied cheaply to the current gradient. This makes the method compatible with standard optimizers and with perturb-and-recompute schemes: SAM determines a local sharpness-aware gradient, while LLQR supplies the anisotropic geometry used to probe and/or transport that gradient.

B Detailed Analysis for the Two-Scale Pothole Model

This appendix contains the supporting arguments used in Sections 3 and 4. The first subsection records the fixed-metric Riemannian-SAM transfer for LLQR +SAM. The remaining subsections justify the two-scale pothole calculation: the coordinate recursion, the scalar hovering envelope, the vanilla-SAM comparison, and the stochastic selection picture.

B.1 Riemannian-SAM transfer under the frozen LLQR metric

This subsection records the convergence-transfer statement used in Section 3. The statement is conditional on the LLQR metric being frozen during each perturb-and-recompute step; it gives stationarity in the instantaneous metric, not in a fixed limiting metric unless additional metric convergence is assumed.

Let $P_t = U_t^{-1}$. Assume that U_t is measurable with respect to the optimization history \mathcal{F}_t , is fixed during the SAM perturb-and-recompute step, and satisfies the uniform spectral bounds

$$0 < u_{\min} I \preceq U_t \preceq u_{\max} I < \infty.$$

Assume also that the smoothness, retraction-Lipschitz, and stochastic-gradient assumptions of Riemannian SAM [Yun and Yang, 2023] hold uniformly for the compact family of metrics $\{P_t\}$.

Proposition B.1 (Riemannian-SAM transfer for LLQR +SAM). *With the same decaying stepsize and perturbation radius schedule as in Riemannian SAM, for $\tau \sim \text{Unif}\{0, \dots, T-1\}$,*

$$\mathbb{E} [\|\text{grad}_{P_\tau} L(\theta_\tau)\|_{P_\tau}^2] = \mathbb{E} [\nabla L(\theta_\tau)^\top U_\tau \nabla L(\theta_\tau)] = O(T^{-1/2}),$$

up to the same stochastic-gradient and minibatch-variance terms as in the Riemannian-SAM theorem. Consequently,

$$\mathbb{E} \|\nabla L(\theta_\tau)\|_2^2 = O(T^{-1/2}).$$

Proof. Condition on \mathcal{F}_t . Since U_t is \mathcal{F}_t -measurable and fixed during the perturb-and-recompute step, $P_t = U_t^{-1}$ is a fixed Riemannian metric for the current update. For the constant metric

$$\langle \xi, \zeta \rangle_{P_t} = \xi^\top P_t \zeta,$$

the Riemannian gradient is

$$\text{grad}_{P_t} L(\theta) = P_t^{-1} \nabla L(\theta) = U_t \nabla L(\theta),$$

and hence

$$\|\text{grad}_{P_t} L(\theta)\|_{P_t}^2 = \nabla L(\theta)^\top U_t \nabla L(\theta).$$

The LLQR + SAM perturbation

$$\epsilon_t = \rho_t \frac{U_t g_t}{(g_t^\top U_t g_t)^{1/2}}$$

is therefore the normalized Riemannian steepest-ascent direction under the frozen metric P_t . The update

$$\theta_{t+1} = \theta_t - \alpha_t U_t \nabla L_{b_t}(\theta_t + \epsilon_t)$$

is the corresponding Riemannian steepest-descent step on the probed loss. Conditioned on \mathcal{F}_t , this is one fixed-metric Riemannian-SAM step.

The spectral bounds on U_t place all metrics $P_t = U_t^{-1}$ in a compact subset of the positive-definite cone. Hence the norm-equivalence, smoothness, retraction-Lipschitz, and stochastic-gradient constants in the Riemannian-SAM one-step descent inequality can be chosen uniformly over t . Applying that inequality conditionally on \mathcal{F}_t , then taking expectation and summing over $t = 0, \dots, T-1$, gives

$$\frac{1}{T} \sum_{t=0}^{T-1} \mathbb{E} \|\text{grad}_{P_t} L(\theta_t)\|_{P_t}^2 = O(T^{-1/2}),$$

up to the same stochastic-gradient and minibatch-variance terms. Equivalently, for $\tau \sim \text{Unif}\{0, \dots, T-1\}$,

$$\mathbb{E} \|\text{grad}_{P_\tau} L(\theta_\tau)\|_{P_\tau}^2 = O(T^{-1/2}).$$

Finally, since $U_t \succeq u_{\min} I$,

$$\nabla L(\theta_t)^\top U_t \nabla L(\theta_t) \geq u_{\min} \|\nabla L(\theta_t)\|_2^2,$$

so stationarity in the instantaneous *LLQR* metric implies Euclidean first-order stationarity:

$$\mathbb{E} \|\nabla L(\theta_\tau)\|_2^2 \leq u_{\min}^{-1} \mathbb{E} [\nabla L(\theta_\tau)^\top U_\tau \nabla L(\theta_\tau)] = O(T^{-1/2}).$$

If $U_t \rightarrow U_f$ and $\|\nabla L(\theta_t)\|_2 \leq G$, then

$$|\nabla L(\theta_t)^\top U_t \nabla L(\theta_t) - \nabla L(\theta_t)^\top U_f \nabla L(\theta_t)| \leq G^2 \|U_t - U_f\|_{\text{op}}.$$

Averaging gives

$$\frac{1}{T} \sum_{t=0}^{T-1} \mathbb{E} [\nabla L(\theta_t)^\top U_f \nabla L(\theta_t)] \leq O(T^{-1/2}) + G^2 \frac{1}{T} \sum_{t=0}^{T-1} \mathbb{E} \|U_t - U_f\|_{\text{op}}.$$

Thus convergence in the limiting metric follows whenever this average discrepancy vanishes, and the original rate is preserved when the discrepancy is $O(T^{-1/2})$. \square

B.2 Whitened form and non-commuting case

The commuting hypothesis used in the main text is not essential. Define

$$y_t := \bar{H}^{1/2} e_t, \quad A := \bar{H}^{-1/2} H \bar{H}^{-1/2} = I + \bar{H}^{-1/2} H_e \bar{H}^{-1/2}.$$

Since $A \succ 0$ is symmetric, it admits an orthonormal eigendecomposition. Its eigenvalues are the perceived sharpnesses μ_i . In the commuting case, these reduce to

$$\mu_i = \frac{\lambda_i}{\bar{\lambda}_i} = 1 + \frac{\lambda_{\epsilon,i}}{\bar{\lambda}_i}.$$

Using $U = \bar{H}^{-1}$, the exact LLQR+SAM recursion becomes, in whitened coordinates,

$$y_{t+1} = (I - \eta A) y_t - \frac{\eta \rho}{\|A y_t\|_2} A^2 y_t. \quad (10)$$

Thus the non-commuting case is identical after diagonalizing the normalized curvature matrix A . The shared-eigenbasis presentation in the main text is only a notational simplification.

B.3 Coordinate recursion

For the quadratic loss $L(\theta) = \frac{1}{2} \theta^\top H \theta$, we have $g(\theta) = H \theta$. The LLQR+SAM perturbation gives

$$g(\theta^+) = H \theta + \rho \frac{H U H \theta}{\|H \theta\|_U},$$

and therefore, with $e_t = \theta_t$,

$$e_{t+1} = (I - \eta U H) e_t - \frac{\eta \rho}{\|H e_t\|_U} U H U H e_t. \quad (11)$$

In the commuting case, let v_i be the common eigenvectors of \bar{H} , H_e , and H , and write $e_t = \sum_i z_{i,t} v_i$. Since

$$\bar{H} v_i = \bar{\lambda}_i v_i, \quad H v_i = \lambda_i v_i,$$

we get

$$U H v_i = \bar{H}^{-1} H v_i = \frac{\lambda_i}{\bar{\lambda}_i} v_i = \mu_i v_i, \quad U H U H v_i = \mu_i^2 v_i.$$

Moreover,

$$\|H e_t\|_U^2 = (H e_t)^\top U (H e_t) = \sum_j \lambda_j^2 \bar{\lambda}_j^{-1} z_{j,t}^2 = \sum_j \mu_j^2 \bar{\lambda}_j z_{j,t}^2.$$

Substituting these identities into (11) gives the full coordinate recursion

$$z_{i,t+1} = (1 - \eta \mu_i) z_{i,t} - \frac{\eta \rho \mu_i^2}{\sqrt{\sum_j \mu_j^2 \bar{\lambda}_j z_{j,t}^2}} z_{i,t}. \quad (12)$$

If one eigendirection v_i dominates, the denominator reduces to $\mu_i \sqrt{\bar{\lambda}_i} |z_{i,t}|$, yielding the scalar recursion

$$z_{i,t+1} = (1 - \eta \mu_i) z_{i,t} - \frac{\eta \rho \mu_i}{\sqrt{\bar{\lambda}_i}} \text{sign}(z_{i,t}). \quad (13)$$

This is the one-dimensional model used in the main text.

B.4 Scalar Hovering Envelope

Consider the scalar map

$$z_{t+1} = az_t - b \operatorname{sign}(z_t), \quad a \in (0, 1), \quad b > 0. \quad (14)$$

It has no nonzero fixed point. Indeed, if $z > 0$, then

$$z = az - b \implies z = -\frac{b}{1-a} < 0,$$

which contradicts $z > 0$; the negative half-line gives the symmetric contradiction. Hence the map cannot localize at a nonzero point and instead oscillates around the origin.

Once the signs alternate, the limiting two-cycle has amplitude r_* satisfying

$$r_* = b - ar_*,$$

so

$$r_* = \frac{b}{1+a}. \quad (15)$$

For (13),

$$a_i = 1 - \eta\mu_i, \quad b_i = \frac{\eta\rho\mu_i}{\sqrt{\bar{\lambda}_i}},$$

and therefore the exact asymptotic two-cycle amplitude is

$$\limsup_{t \rightarrow \infty} |z_{i,t}| = \frac{b_i}{1+a_i} = \frac{\eta\rho\mu_i}{(2-\eta\mu_i)\sqrt{\bar{\lambda}_i}}. \quad (16)$$

The main text uses the simpler hovering envelope

$$|z_{i,t}| \lesssim \frac{b_i}{1-a_i} = \frac{\rho}{\sqrt{\bar{\lambda}_i}}. \quad (17)$$

This envelope is the scale relevant for the cancellation argument: the SAM kick b_i and the contraction scale $1 - a_i = \eta\mu_i$ both grow linearly with the perceived sharpness μ_i , leaving a radius controlled only by the average curvature $\bar{\lambda}_i$.

B.5 Pothole Escape Criterion

The quadratic model is local, so it does not by itself describe the global motion after leaving a well. It gives a localization criterion. If a pothole has basin radius r_ϵ in the relevant eigendirection, then the local model predicts loss of localization when the hovering envelope exceeds that radius:

$$\frac{\rho}{\sqrt{\bar{\lambda}_\epsilon}} > r_\epsilon. \quad (18)$$

The key point is that this criterion depends on the average curvature $\bar{\lambda}_\epsilon$, not on the localized pothole sharpness λ_ϵ . A sharper localized component increases the perceived sharpness μ_ϵ , but the SAM kick and contraction scale increase together, producing the cancellation in (17).

In a wide basin, small $\bar{\lambda}_i$ is paired with a large basin radius, so the same envelope can remain inside the basin. In a pothole, the basin radius is small while the average direction remains flat, so the same envelope can exceed the local basin radius.

B.6 Vanilla SAM Comparison

For vanilla SAM, $U = I$. In an eigendirection of H , the scalar recursion is

$$z_{t+1} = (1 - \eta\lambda_i)z_t - \eta\rho\lambda_i \operatorname{sign}(z_t). \quad (19)$$

The same envelope calculation gives

$$\frac{\eta\rho\lambda_i}{\eta\lambda_i} = \rho. \quad (20)$$

Thus vanilla SAM has a Euclidean hovering envelope of order ρ in every direction, whereas LLQR+SAM has the direction-dependent envelope $\rho/\sqrt{\bar{\lambda}_i}$.

Corollary B.2 (Pothole-escape amplification). *Under Assumption 4.1 and the commuting hypothesis, the LLQR+SAM hovering envelope around a pothole minimum is*

$$\frac{\rho}{\sqrt{\bar{\lambda}_\epsilon}} = \frac{1}{\sqrt{\lambda_\epsilon}} \times (\text{vanilla-SAM hovering envelope}).$$

The amplification depends only on the average curvature $\bar{\lambda}_\epsilon$ in the pothole direction, not on the localized pothole sharpness λ_ϵ .

This amplification cannot be reproduced selectively by retuning vanilla SAM. Choosing

$$\rho^{\text{SAM}} = \frac{\rho}{\sqrt{\bar{\lambda}_\epsilon}}$$

would match the pothole-direction envelope, but it would enlarge the probe in all directions, including non-pothole directions where this extra scale is not needed. The contraction behavior also differs: vanilla SAM contracts at rate $1 - \eta\lambda_i$, so its stable step size is constrained by the largest curvature of H . LLQR+SAM contracts at rate $1 - \eta\mu_i$, which removes the conditioning of the average geometry \bar{H} from this constraint.

B.7 Stochastic Selection Between Wells

The deterministic calculation above gives a local non-localization criterion: when the hovering envelope is comparable to the radius of a sharp well, the SAM kick prevents long residence near its bottom. With stochastic gradients, this becomes a selection effect. Noise may inject the iterate into a sharp well, but the SAM-induced hovering ejects it quickly; wide flat wells support longer visits because their basin radius is large relative to the hovering scale.

The following regenerative model formalizes this interpretation. It is not intended as a full global model of training dynamics; it isolates the residence-time consequence of the local escape criterion.

Proposition B.3 (Regenerative selection between wells). *Consider a regenerative idealization with wells indexed by m . At each cycle, a well J_n is sampled from a distribution ν with positive mass on each well; the process starts near the well center, evolves under local gradient-noise dynamics with noise scale σ , and exits when $\|e_t\| \geq R$. Suppose flat wells satisfy*

$$\mathbb{E}[\tau_R^{(m)}] \geq c_m^{\text{flat}} R^2 \sigma^{-2},$$

whereas sharp unstable wells satisfy

$$\mathbb{E}[\tau_R^{(m)}] \leq C_m^{\text{sharp}} (1 + \log(R/\sigma)).$$

If at least one flat well is present, then the long-run occupation mass of sharp wells satisfies

$$\sum_{m \in \mathcal{M}_{\text{sharp}}} \mu_m(\sigma) = O\left(\frac{\sigma^2 \log(R/\sigma)}{R^2}\right) \xrightarrow{\sigma \rightarrow 0} 0.$$

Proof. By the renewal-reward formula,

$$\mu_m(\sigma) = \frac{\nu_m \mathbb{E}[\tau_R^{(m)}]}{\sum_\ell \nu_\ell \mathbb{E}[\tau_R^{(\ell)}]}.$$

The total sharp-well numerator is $O(1 + \log(R/\sigma))$, while the denominator is at least the contribution of one flat well, namely $\Omega(R^2 \sigma^{-2})$. Dividing gives the stated bound. \square

For a pothole direction, the relevant dimensionless escape ratio is

$$\frac{\rho}{r_\epsilon \sqrt{\bar{\lambda}_\epsilon}}.$$

Corollary B.2 increases this ratio for LLQR +SAM relative to vanilla SAM, predicting shorter visits to sharp wells and faster selection of the wide flat basin.

The next calculation supports the path-length behavior observed in the noisy toy experiment. It states that, in a stable scalar noisy mode, increasing the effective metric denominator damps both stationary variance and one-step motion.

Proposition B.4 (Metric damping under gradient noise). *Consider the scalar noisy recursion*

$$z_{t+1}^B = q_i^B z_t^B - \eta(d_i^B)^{-1} \varepsilon_{i,t}, \quad q_i^B := 1 - \eta\lambda_i(d_i^B)^{-1}, \quad \text{Var}(\varepsilon_{i,t}) = \tau_i^2,$$

where B denotes a metric choice and $d_i^B > \eta\lambda_i/2$. Then

$$\text{Var}_{\pi_B}(z_i) = \frac{\eta\tau_i^2}{\lambda_i(2d_i^B - \eta\lambda_i)}, \quad \mathbb{E}_{\pi_B}[(z_{i,t+1}^B - z_{i,t}^B)^2] = \frac{2\eta^2\tau_i^2}{d_i^B(2d_i^B - \eta\lambda_i)}.$$

Consequently, if $d_i^P \geq d_i^Q > \eta\lambda_i/2$, then metric P has no larger stationary variance or one-step motion than metric Q , with strict improvement when $\tau_i^2 > 0$ and $d_i^P > d_i^Q$.

Proof. The AR(1) variance equation gives

$$V_i^B = (q_i^B)^2 V_i^B + \frac{\eta^2 \tau_i^2}{(d_i^B)^2}.$$

Since

$$1 - (q_i^B)^2 = \frac{\eta\lambda_i(2d_i^B - \eta\lambda_i)}{(d_i^B)^2},$$

we obtain

$$V_i^B = \frac{\eta\tau_i^2}{\lambda_i(2d_i^B - \eta\lambda_i)}.$$

Moreover,

$$z_{i,t+1}^B - z_{i,t}^B = -\eta\lambda_i(d_i^B)^{-1} z_{i,t}^B - \eta(d_i^B)^{-1} \varepsilon_{i,t}.$$

At stationarity, $z_{i,t}^B$ is independent of the fresh noise, so the cross term vanishes and

$$\mathbb{E}_{\pi_B}[(z_{i,t+1}^B - z_{i,t}^B)^2] = \frac{\eta^2}{(d_i^B)^2} (\lambda_i^2 V_i^B + \tau_i^2) = \frac{2\eta^2\tau_i^2}{d_i^B(2d_i^B - \eta\lambda_i)}.$$

Both denominators are increasing for $d_i^B > \eta\lambda_i/2$, which proves the comparison. \square

C Experiments Details

C.1 Standard Supervised Training Benchmarks

CIFAR protocol. For CIFAR-10 and CIFAR-100, all methods use the same supervised classification protocol: a 200-epoch cosine schedule with initial learning rate 0.05, Polyak momentum 0.9, batch size 128, random crop and horizontal flip augmentation, normalization, and Cutout regularization [Devries and Taylor, 2017]. Weight decay is selected in $\{10^{-4}, 5 \times 10^{-4}, 10^{-3}\}$ based on baseline best performance. SAM uses the recommended perturbation radius $\rho = 0.1$ on CIFAR-10 and $\rho = 0.2$ on CIFAR-100 [Foret et al., 2021, Li and Giannakis, 2023, Mi et al., 2022, Li et al., 2024]; FisherSAM uses its recommended $\rho = 0.1$ and inverse-Fisher regularization $\eta = 0.1$ [Kim et al., 2022]. The LLQR rows keep the outer SGDM recipe fixed and use the recommended inner preconditioner-learning settings of Dufort-Labbé et al. [2026]: inner batch size 128, preconditioner learning rate 10^{-3} , 50 inner momentum-solver steps, and update period 500 optimizer steps. The reported NGD rows use the NGD-induced divergence with EMA 0.95, while the Newton rows use the Newton-induced divergence with EMA 0.9. LLQR+SAM reuses the same hyperparameters as its LLQR and SAM components, without additional method-specific tuning. Each CIFAR entry is the best test accuracy observed during training, aggregated over five independent seeds. All CIFAR experiments were run on NVIDIA L40S GPUs.

TinyImageNet protocol. TinyImageNet-200 uses the same training and reporting protocol and optimizer hyperparameters as the CIFAR benchmarks, with the comparison restricted in the main text to ResNet-18 and WRN-28-10. Entries in Table 3 are best top-1 test accuracy aggregated over three seeds. All TinyImageNet experiments were run on NVIDIA L40S GPUs.

SAM-variant synergy protocol. The CIFAR SAM-variant comparison pairs LLQR with F-SAM [Li et al., 2024]. F-SAM uses the recommended exponential moving average of gradient accumulation: $\lambda = 0.9$ for WRN-28-10 and PyramidNet-110, and $\lambda = 0.6$ for the other architectures. The comparison otherwise follows the CIFAR protocol above and reports best top-1 test accuracy over five seeds. All experiments were run on NVIDIA L40S GPUs.

ImageNet protocol. The ImageNet comparison uses ResNet-50 on ImageNet [Deng et al., 2009]. Relative to the preceding vision experiments, the only hyperparameter changes are $\rho = 0.075$ and $\lambda = 0.95$, following the recommendation of Li et al. [2024]. The LLQR rows use the E-KFAC block structure. All ImageNet experiments were run on NVIDIA A100 GPUs.

IWSLT14 German-to-English protocol. The sequence-modeling benchmark uses the fairseq IWSLT14 German-to-English Transformer training recipe of Ott et al. [2018]. The SAM perturbation radius is tuned over $[0.0005, 0.2]$, with $\rho = 0.005$ giving the best validation result. SAM perturbation only starts being applied after learning rate warmup phase for stability. LLQR hyperparameters are kept unchanged from the vision experiments except for the preconditioner EMA decay, which is set to 0.925. Table 6 reports best validation BLEU aggregated over five seeds. All IWSLT14 experiments were run on NVIDIA L40S GPUs.

Table 8: Robustness to symmetric training-label corruption on CIFAR-100. Entries are best test accuracy on clean test labels (mean \pm std, 3 seeds). The corruption rate γ denotes the fraction of randomly flipped training labels. Blue denotes NGD-induced LLQR geometry.

Dataset	γ	Base geometry			Sharpness baseline	Combined geometry and sharpness
		SGDM	ADAM	LLQR	SAM	LLQR+SAM
CIFAR-100	0.2	63.41 \pm 0.46	41.01 \pm 0.63	64.32 \pm 0.22	67.15 \pm 0.43	68.64 \pm 0.36
CIFAR-100	0.6	41.21 \pm 1.27	9.76 \pm 1.46	41.21 \pm 1.13	46.81 \pm 1.46	48.54 \pm 0.81
CIFAR-100	0.7	32.52 \pm 0.72	4.16 \pm 0.52	34.51 \pm 0.71	38.96 \pm 0.72	43.27 \pm 0.82
CIFAR-100	0.8	22.97 \pm 0.86	2.23 \pm 0.12	24.54 \pm 0.46	31.19 \pm 1.74	33.06 \pm 1.22

D Additional Experimental Results

D.1 Noise injection robustness

Since SAM is known to improve robustness under label noise, we ask whether learned geometry strengthens this effect. On CIFAR-100, we corrupt only the training labels with symmetric random flips at rate γ , keep the test set clean, and reuse the standard supervised training recipe. Table 8 reports the best clean-test accuracy across $\gamma \in \{0.2, 0.6, 0.7, 0.8\}$. LLQR+SAM improves over SAM at every corruption level, with especially clear gains at moderate-to-high noise, showing that transporting the sharpness-aware update through the learned LLQR geometry strengthens robustness under corrupted supervision. The gains remain positive even at $\gamma = 0.8$, where supervision is nearly degenerate, the learned-geometry sharpness correction remains beneficial.

D.2 Scalability

Our LLQR implementation attaches a blockwise preconditioner to network layers. The storage footprint is therefore determined by the chosen parameterization of each block rather than by LLQR as a framework. Richer blocks can encode more geometry but require more optimizer state, while simpler parameterizations reduce memory at the cost of expressivity. Table 9 summarizes the resulting fp32 storage across ViT scales for the preconditioner families considered in this scalability study.

For comparison, we also include a hypothetical `diag-krac` structure, which approximates each Kronecker factor by its diagonal: $\text{Diag}(a) X \text{Diag}(b)$ for a reshaped kernel $X \in \mathbb{R}^{m \times n}$. This reduces the per-kernel preconditioner storage from dense Kronecker-style scaling to $O(m + n)$ scalars, providing a lightweight option for trading geometric expressivity for memory.

We also provide cadence results in Table 10 and Fig. 5, to be read as wall-clock overhead measurements, not as accuracy or convergence comparisons. As expected, the cost decreases when LLQR updates are performed less frequently, since fewer preconditioner refreshes are executed per epoch. This steady-update scaling trend is further exposed in Fig. 6.

Table 9: Cross-model analytical fp32 storage for e-KFAC and diag-KFAC preconditioners under ImageNet-scale ViT geometry. Model counts include heads and classification layers; #precond reports the number of stored preconditioner scalars for each parameterization.

Model	Storage	S	#model params	#precond params	precond (MiB/dev.)	total (MiB/dev.)
ViT-Ti/16	e-kfac	1	5,427,080	24,235,082	92.45	113.15
ViT-Ti/16	e-kfac	4	5,427,080	24,235,082	23.11	43.82
ViT-Ti/16	diag-kfac	1	5,427,080	73,426	0.28	20.98
ViT-Ti/16	diag-kfac	4	5,427,080	73,426	0.07	20.77
ViT-B/16	e-kfac	1	86,567,656	387,826,882	1,479.44	1,809.67
ViT-B/16	e-kfac	4	86,567,656	387,826,882	369.86	700.09
ViT-B/16	diag-kfac	1	86,567,656	294,038	1.12	331.35
ViT-B/16	diag-kfac	4	86,567,656	294,038	0.28	330.51
ViT-L/16	e-kfac	1	304,326,632	1,367,114,178	5,215.13	6,376.04
ViT-L/16	e-kfac	4	304,326,632	1,367,114,178	1,303.78	2,464.70
ViT-L/16	diag-kfac	1	304,326,632	771,990	2.94	1,163.86
ViT-L/16	diag-kfac	4	304,326,632	771,990	0.74	1,161.65

Table 10: Measured LLQR cadence details for ViT-B/16 and ViT-L/16. Times are compile-adjusted seconds per epoch, excluding the first preconditioner-update overhead. Baseline rows report first-order optimizer runtimes; LLQR rows additionally report ratios relative to SGD and SAM on the same architecture.

Arch	Method	Update interval	Updates	Epoch time	vs. SGD	vs. SAM	Steady update
ViT-B/16	SGD	–	–	33.20	1.00×	0.35×	–
ViT-B/16	AdamW	–	–	38.51	1.16×	0.41×	–
ViT-B/16	SAM	–	–	93.84	2.83×	1.00×	–
ViT-B/16	LLQR	50	32	1007.31	30.34×	10.73×	59.38
ViT-B/16	LLQR	100	16	408.09	12.29×	4.35×	44.25
ViT-B/16	LLQR	200	8	204.11	6.15×	2.18×	39.38
ViT-B/16	LLQR	500	4	118.97	3.58×	1.27×	38.85
ViT-B/16	LLQR	1000	2	143.95	4.34×	1.53×	86.55
ViT-B/16	LLQR	1500	2	91.24	2.75×	0.97×	42.52
ViT-B/16	LLQR+SAM	50	32	813.98	24.51×	8.67×	46.05
ViT-B/16	LLQR+SAM	100	16	390.59	11.76×	4.16×	39.91
ViT-B/16	LLQR+SAM	200	8	426.81	12.85×	4.55×	85.33
ViT-B/16	LLQR+SAM	500	4	155.50	4.68×	1.66×	40.58
ViT-B/16	LLQR+SAM	1000	2	173.25	5.22×	1.85×	87.41
ViT-B/16	LLQR+SAM	1500	2	112.65	3.39×	1.20×	41.63
ViT-L/16	SGD	–	–	62.59	1.00×	0.43×	–
ViT-L/16	AdamW	–	–	67.84	1.08×	0.46×	–
ViT-L/16	SAM	–	–	146.54	2.34×	1.00×	–
ViT-L/16	LLQR	50	32	1647.13	26.32×	11.24×	97.46
ViT-L/16	LLQR	100	16	868.47	13.88×	5.93×	97.34
ViT-L/16	LLQR	200	8	476.77	7.62×	3.25×	97.52
ViT-L/16	LLQR	500	4	275.63	4.40×	1.88×	95.18
ViT-L/16	LLQR	1000	2	299.48	4.79×	2.04×	96.46
ViT-L/16	LLQR	1500	2	301.14	4.81×	2.06×	95.91
ViT-L/16	LLQR+SAM	50	32	1809.84	28.92×	12.35×	95.78
ViT-L/16	LLQR+SAM	100	16	914.70	14.62×	6.24×	96.36
ViT-L/16	LLQR+SAM	200	8	667.77	10.67×	4.56×	96.20
ViT-L/16	LLQR+SAM	500	4	470.89	7.52×	3.21×	96.57
ViT-L/16	LLQR+SAM	1000	2	238.29	3.81×	1.63×	96.11
ViT-L/16	LLQR+SAM	1500	2	372.23	5.95×	2.54×	95.50